ACS Sustainable Chemistry & Engineering

Research Article

Cite This: ACS Sustainable Chem. Eng. 2018, 6, 15487−15493

pubs.acs.org/journal/ascecg

Control of Electrical and Thermal Transport Properties by Hybridization of Two-Dimensional Tungsten Disulfide and Reduced Graphene Oxide for Thermoelectric Applications

Soohyun Kim, Hyunwoo Bark, Seungjin Nam, Hyunjoo Choi, and Hyunjung Lee*

School of Advanced Materials Engineering, Kookmin Univ., 77, Jeongneung-ro, Seongbuk-gu, Seoul, Republic of Korea

Supporting Information

ABSTRACT: Thermoelectric efficiency is determined by the figure of merit (ZT) with the achievement of high electrical conductivity (σ), high Seebeck coefficient (S), and low thermal conductivity (k) for high performance thermoelectric devices. Tungsten disulfide (WS_2) has been reported to have a comparably high S (3.5×10^2~9.5×10^2 μV/K) and low σ (10^{-2}−10^{-1} S/m), which leads to a low ZT value (approximately 0). In this study, WS_2 particles were hybridized with highly conductive reduced graphene oxide (rGO) particles (~10^5 S/m). The inclusion of rGO provides conductive paths for the transfer of carriers in the composites, and thus, this led to an increase in σ (~3×10^3 S/m). The hybrid material of WS_2/rGO, as a function of the weight percentage of rGO, was fabricated by spark plasma sintering. As a result, the power factor in a WS_2/0.8 wt % rGO (87 μW/mK^2) with enhanced σ was 310% greater than that of WS_2. Moreover, two-dimensional structures of the materials contributed to the induction of phonon scattering and resulted in steady k in spite of enhanced σ with increased rGO content. Consequently, an optimized ZT value was obtained for the WS_2/0.8 wt % rGO sample; this value was 260% greater (approximately 6.8×10^{-4}) than that of WS_2 without rGO (approximately 1.9×10^{-4}).

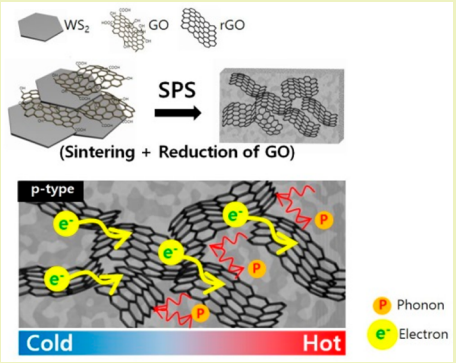

KEYWORDS: *Thermoelectric material, Tungsten disulfide (WS2), Reduced graphene oxide (rGO), Organic−inorganic composite, Spark plasma sintering (SPS)*

INTRODUCTION

Thermoelectric power generation devices convert thermal energy to electrical energy. As the devices are environmentally friendly and also increase energy efficiency by using waste thermal energy, they are regarded as new and renewable energy devices.[1,2] These devices are being trialed in various applications, including in vehicles, in fabrics, and as hybrids with other energy devices.[3−5] The performance of thermoelectric power generation is determined by the figure of merit (ZT) in eq 1, which is dependent upon the Seebeck coefficient (S), electrical conductivity (σ), and thermal conductivity (k). Optimization of these three factors is important for a high ZT value but is very complicated to achieve because of interdependent relationship of the three impact factors with carrier concentration, mobility, electronic structure, and lattice structure.[6] Many studies have tried to optimize the ZT value and to achieve highly efficient thermoelectric materials through independent control of each factor.[7−11]

$$\mathrm{ZT} = \frac{S^2 \sigma T}{k} \quad (1)$$

Tungsten disulfide (WS_2) has recently emerged as a promising thermoelectric material. WS_2, one of the transition-metal dichalcogenides, is a p-type two-dimensional semiconductor material. This material has a layered structure comprising a lot of nanosheets, which is the preferred method to confine carriers and to obstruct transport of vibrating phonons. One of the reported characteristics of this structure is that it has a high Seebeck coefficient (3.5×10^2~9.5×10^2 μV/K) and a low thermal conductivity (6.5×10^{-1}−6.0×10^{0} W/mK). Despite these advantages as thermoelectric material, WS_2 has a low ZT value (10^{-5}−10^{-3} at 300−800 K) because of its relatively low electrical conductivity (10^{-2}−10^{1} S/m).[12−14] WS_2 is also nontoxic and stable at high temperatures; this is in contrast to Bi-based materials, which have typically been studied as efficient thermoelectric materials in many research groups. Some research groups have tried to solve this problem through hybridization with nanocarbon-based materials that generally have high electrical conductivity.[15] Suh et al. obtained 1330%-increased ZT value (2.2×10^{-1}) in a composite of microsized WS_2 particles and multilayer nanotubes (MWNTs) (0.75 wt %) through spark plasma sintering (SPS).[16]

To overcome low electrical conductivity of WS_2, WS_2 was hybridized with reduced graphene oxide (rGO) as a conductive material in this study, and their electrical and

Received: August 10, 2018
Revised: September 22, 2018
Published: September 28, 2018

DOI: 10.1021/acssuschemeng.8b03949
ACS Sustainable Chem. Eng. 2018, 6, 15487−15493

thermal transport behaviors were studied. The hybrid material of WS_2/rGO was fabricated by SPS at 1473 K as a function of the composition of rGO (wt %). During SPS process, sintering of WS_2 particles and reduction of GO were formed. High-temperature treatment (~1473 K) in vacuum was enough to reduce GO with high crystalline quality, leading to an effective restoration of the conductivity with removal of oxygen functional groups.[17−19] Accordingly, it was expected that the rGO provides an effective conductive path for the transport of charge carriers in WS_2/rGO composites, and their thermoelectric property increases while maintaining a low carrier concentration of the matrix of WS_2. In addition, as the 2D structure of WS_2 and rGO effectively provides a large surface area, hybridization of these materials was expected to induce phonon scattering at the interface between the two materials in the composites, resulting in independently low thermal conductivity to electrical conductivity. As a result, carrier mobility and concentration were increased by hybridizing with rGO, resulting in enhanced electrical conductivity in the composite indicating at least 500 times larger than those of WS_2. Moreover, thermal conductivity remained at the level of that of WS_2 without rGO (about 40 W/mK) because of the 2D structure of the materials in spite of increased rGO content. As a result of these properties, the optimized ZT value of the composite was found in WS_2/0.8 wt % rGO sample, which was increased by 260% as compared with that of the WS_2.

RESULTS AND DISCUSSION

Scheme 1 describes the schematics of the overall experimental process. The filtered powders of WS_2 and GO were sintered by

Scheme 1. Schematic Diagram of the Experimental Procedure

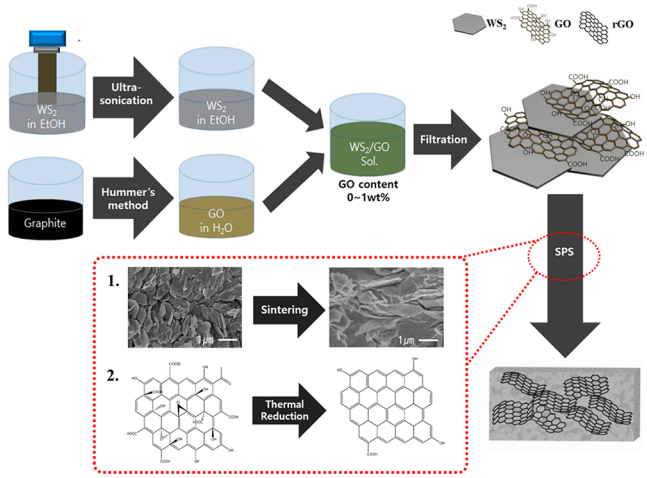

SPS, and the GO nanosheets were reduced thermally simultaneously. GO, WS_2, and their mixed solutions were highly dispersed, as shown in Figure 1a. In Figure 1b, atomic force microscopy (AFM) images show that the GO nanosheets have a lateral size of approximately above 1 μm and a thickness of 1.3−1.6 nm. Considering that the thickness of the monolayer GO is reported to be approximately 6 Å, it can be seen that the GO nanosheets have two or three layers.[20] Figure 1c shows WS_2 particles before mixing with GO. Well-dispersed WS_2/GO hybridized particles are shown in Figure 1d. GO nanosheets were stacked on the WS_2 particles, thereby connecting the organic and inorganic compounds. Figure 1e and f shows the morphology of WS_2/rGO composite after the SPS process. The dispersion of rGO nanosheets was observed by energy-dispersive system (EDS) mapping. We found that carbon elements were spread evenly in the whole area while the rGO nanosheets were highly dispersed with stacking on each WS_2 particle.

Figure 2 shows the diffraction pattern of pristine WS_2, SPS-sintered WS_2, and WS_2/rGO composites. After SPS processing, 2H-WS_2 (hexagonal phase) was observed in both WS_2 and WS_2/1 wt % rGO composites. In the SPS-sintered WS_2 sample, significant peaks were observed at 39.45° and 49.60°, which would indicate a growth of the (103) and (105) planes, respectively. Growth of these planes, however, was restricted to the WS_2/1 wt % rGO sample because of rGO nanosheets.[21,22] In addition, minor peaks were observed for sulfur (S, 18.55° and 21.35°) and tungsten carbide (WC, 31.45°, 48.25°, and 63.95°) in WS_2/1 wt % rGO sample, as indicated by the diamond and circle symbols, respectively. Considering that the decomposition temperature of WS_2 is reported to be 1313~1533 K with high thermal stability,[23,24] the high temperature of the SPS process in this experiment (1473 K) might have had a slight effect on the decomposition of WS_2. Moreover, it is reported that the nucleation and growth of WC in the composite was formed during the thermal annealing at temperatures above 1073 K.[25,26] Carbon atoms from GO were easily diffused into vacancies in WS_2 particles at high temperature.[27] This may have led to the formation of WC during SPS. However, when the existence of WC peaks was checked through Raman spectra, it was not found in the Raman spectra of WS_2/5wt % rGO, despite relatively high rGO content (Figure 3); the characteristic peaks for WC are reported to be observed at 267, 716, and 805 cm^{-1} in Raman spectra.[28] So, we found that the formation of WC had a negligible influence on the formation of the WS_2/rGO composites.

Also, the reduction of the dispersed GO nanosheets after the SPS process was confirmed by Raman spectra, as shown in Figure 3. In Figure 3a, strong peaks of $E^1_{2g}(\Gamma)$ and $A_{1g}(\Gamma)$ at 351.25 and 420.86 cm^{-1} occur from WS_2, indicating in-plane and out-of-plane vibrational mode of sulfur atom in WS_2 and observed in both before and after SPS treated samples.[29,30] Significant change was shown before and after SPS process at 1300−3000 cm^{-1} regions in which peaks occur from graphene structures. In the Raman spectra of graphene structure, the G peak (~1580 cm^{-1}) was revealed by sp^2-hybridized bonding in carbon materials, and the D peak (~1350 cm^{-1}) was activated by lattice vibration at defects or edges of the graphene structures.[31−33] In Figure 3b, the relatively broad G peak before the SPS treated sample shifted from 1596.4 cm^{-1} to 1575.8 cm^{-1} with sharpening of the peak after SPS process.[34,35] This means that GO was successfully reduced by thermal reaction in SPS process at 1473 K. It was also confirmed by the ratio of the D peak to the G peak (I_D/I_G) indicating the degree of the defect in the graphene structure. I_D/I_G for WS_2/5 wt % GO before SPS processing was 1.1, and this ratio was decreased to 0.57 for WS_2/5 wt % rGO after SPS process. In addition, the 2D peak (2854.9 cm^{-1}) was activated by π bonding of crystalline graphitic materials after SPS. These results indicated that thermally reduced GO in this SPS process had high crystalline quality of rGO with reducing the defects by lattice contraction as well as removal of oxide groups such as carboxyl (−COOH), hydroxyl (−OH), and epoxide

DOI: 10.1021/acssuschemeng.8b03949
ACS Sustainable Chem. Eng. 2018, 6, 15487−15493

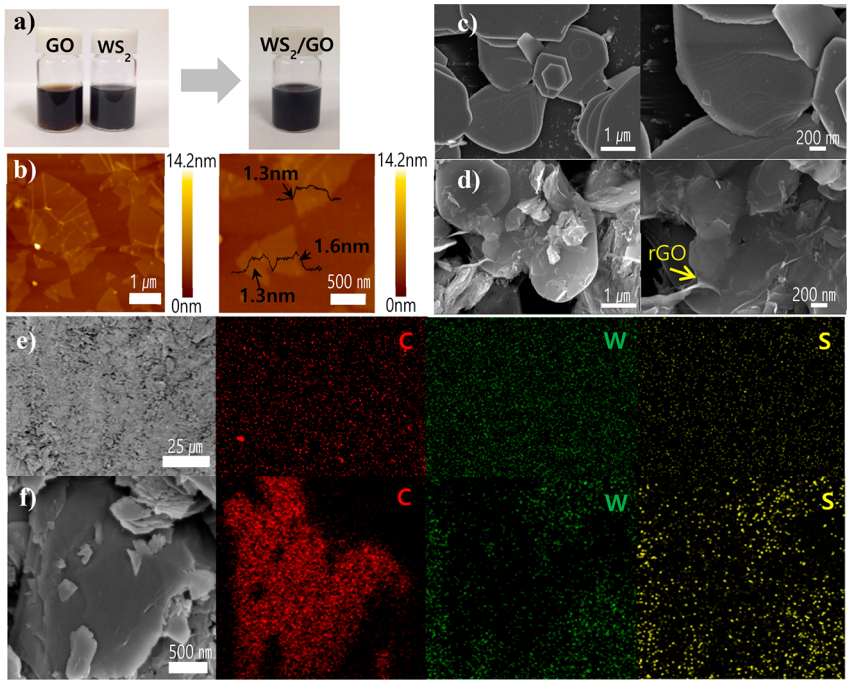

Figure 1. Morphology of each powder and WS_2/rGO composites before and after SPS process: (a) dispersed GO in DIW (1 mg/mL) and WS_2 in EtOH (2 mg/mL) (left) and WS_2/0.5 wt % GO in cosolvent (EtOH and DIW) (right) and (b) AFM images of deposited GO nanosheets on Si wafer. SEM images of (c) WS_2 powder and (d) mixed WS_2/GO powder (WS_2/0.5 wt % GO). (e, f) SEM images and EDS mapping images of fabricated WS_2/GO composite (WS_2/1 wt % rGO) (red, green, and yellow points indicate, respectively, C, W, and S element).

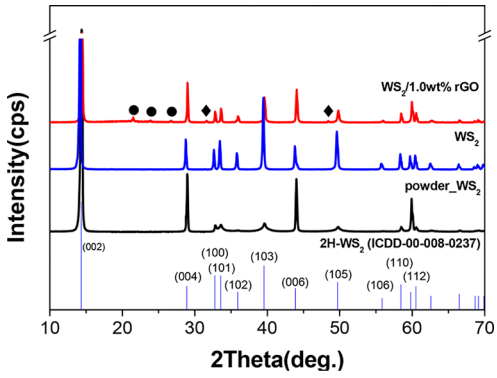

Figure 2. X-ray diffraction (XRD) of WS_2, SPS-sintered WS_2, and WS_2/1 wt % rGO composites. For comparison, diffraction patterns for 2H-WS_2 are shown from the reference (ICDD 00-008-0237). The diamond and circle symbols indicate WC and S, respectively.

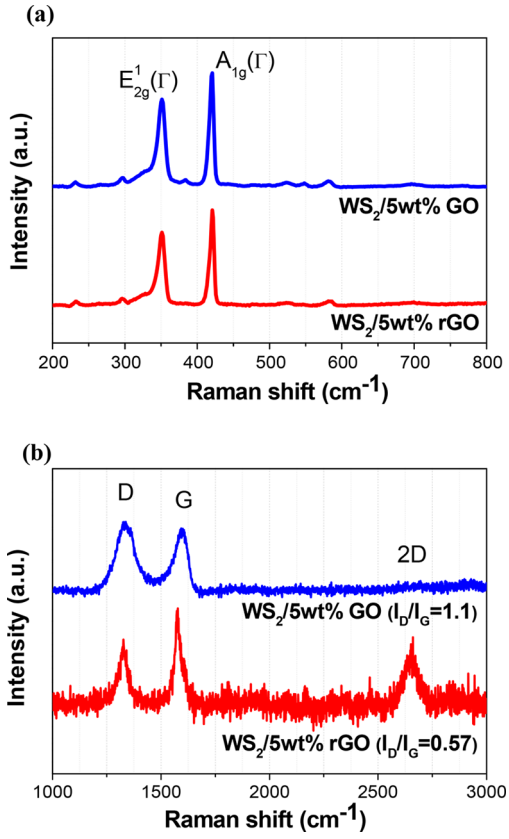

Figure 3. Raman spectra of WS_2/GO and rGO prepared before and after SPS process; (a) $E^1_{2g}(\Gamma)$ and $A_{1g}(\Gamma)$ peaks of WS_2 and (b) D, G, and 2D peaks of graphene structure at each sample of WS_2/5 wt % GO (blue line) and WS_2/5 wt % rGO (red line).

(>O) groups by thermal annealing effect at high temperature of 1473 K in spite of short duration time of 1 min.[19]

With reduced GO and sintering of the composites, we analyzed the behaviors of the majority carriers and the thermoelectric properties as a function of the rGO content in the WS_2/rGO composites after the SPS process in Figure 4. Figure 4a shows the behavior of the carrier concentration and its mobility in WS_2/rGO composites. At a low content of rGO (<0.4 wt %) in composites, major carrier concentration increased by adding rGO in composite films: from 1.1 × 10^{12} cm^{-3} in WS_2 to approximately 3.4 × 10^{17} cm^{-3} in WS_2/0.4 wt % rGO because of carrier-enriched rGO (10^{16}~10^{19} cm^{-3}).[36] The increased value was maintained at 5 wt % rGO content having a relatively constant value (approximately 2 × 10^{17} cm^{-3}). Unlike change behavior of carrier concentration, the mobility was obviously increased by rGO content from 0 to

DOI: 10.1021/acssuschemeng.8b03949
ACS Sustainable Chem. Eng. 2018, 6, 15487−15493

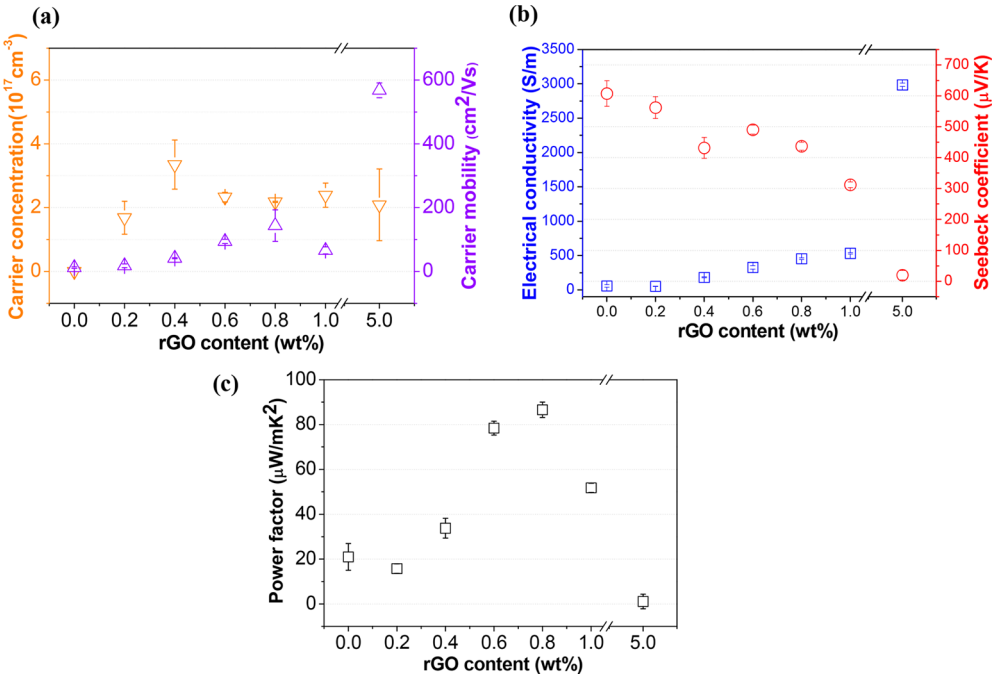

Figure 4. Thermoelectric properties of WS_2/rGO composites with various rGO content: (a) majority carrier concentration (inverted triangle) and mobility (triangle), (b) Seebeck coefficient (S, circle) and electrical conductivity (σ, square), and (c) power factor ($S^2\sigma$ calculated with Seebeck coefficient and electrical conductivity from 0 to 5 wt % rGO content in the composites. The obtained Seebeck coefficient and electrical conductivity were the average value of three independent data.

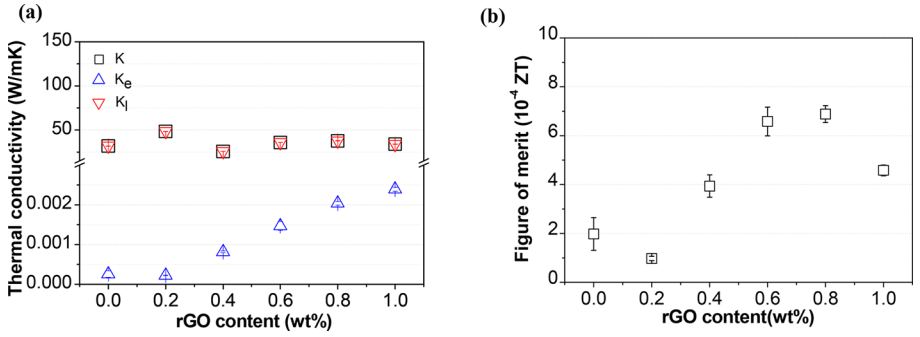

Figure 5. Thermal conductivity and figure of merit (ZT) of WS_2/rGO composites by various rGO content; (a) total thermal conductivity (square), lattice (inverted triangle), and electrical (triangle) parameter in thermal conductivity and (b) ZT value from 0 to 1 wt % rGO content in the composites.

5 wt % (approximately from 12 to 570 cm^2/(V s)) with 4650% of increase. This means that carrier transport paths were formed by percolation rGO nanosheets in the composite.[16,37]

Thermoelectric properties were also changed, reflecting the behavior of carrier concentration and mobility as a function of rGO content. The Seebeck coefficient (S) is known to be inversely proportional to carrier concentration (n) and the effective mass of charge carrier (m^*) such as eq 2 which increased high and sharp density of state (DOS) near the Fermi level (E_F) of the materials. Electrical conductivity (σ), however, is proportional to both carrier concentration (n) and carrier mobility (μ) (e is the charge of electron, 1.6×10^{19} C) (eq 3).[6]

$$S \propto m^* T\left(\frac{\pi}{3n}\right)^{2/3} \quad (2)$$

$$\sigma = ne\mu \quad (3)$$

In the Seebeck coefficient measurement system, ±1 and 3 K of temperature gradient (ΔT) was applied to the end of samples at room temperature (300 K) for measuring difference of potential (ΔV) by the temperature gradient. In the plot of $\Delta V/\Delta T$ (Figure S1), the slope with linear fitting indicated Seebeck coefficient of the samples having no consideration for that of probe material (Pt, S_{pt} = −6.9 μV/K). When the measured Seebeck coefficient and electrical conductivity of the WS_2/rGO composite with various rGO contents were compared with each other in Figure 4b, the Seebeck coefficient decreased from 6.1×10^2 μV/K in WS_2 to 1.9×10^1 μV/K in the WS_2/5 wt % rGO sample with an increase of rGO content. When rGO fraction in the composite was increased, the properties with rGO band structure as semimetallic material with broad and low DOS near E_F had a higher effect on the properties of the composite than that of a composite with low content of rGO.[38] However, electrical conductivity increased from 6.0×10^1 S/m at WS_2 to 3.0×10^3 S/m at WS_2/5 wt % rGO, reflecting the increase of carrier mobility. Consequently,

DOI: 10.1021/acssuschemeng.8b03949
ACS Sustainable Chem. Eng. 2018, 6, 15487−15493

the highest power factor ($S^2\sigma$) was obtained at 0.8 wt % rGO (8.7×10^1 μW/mK^2), as shown in Figure 4c. The value was 310% greater than that of WS_2 (2.1×10^1 μW/mK^2).

As an important factor of thermoelectric properties, thermal conductivity of the WS_2/rGO hybrid materials was analyzed. Table S1 shows the factors as experimental density (ρ), specific heat capacity (c_p), and thermal diffusivity (a) of each sample for calculation of thermal conductivity (eq 4).

$$k = \rho c_p a \tag{4}$$

Interesting behavior is shown in thermal conductivities in Figure 5a. Thermal conductivity (k) comprises the electric factor (k_e) by transport of carriers and the lattice factor (k_l) by traveling phonons in the lattice structure (eq 5) with interdependent relationship. The electric factor is determined by the Widemann−Franz law (eq 6), where L indicates the Lorenz factor (2.4×10^{-8} J^2 K^{-1} C^{2-}, free electrons).[6]

$$k = k_e + k_l \tag{5}$$

$$k_e = L\sigma T \tag{6}$$

As eq 6 indicates that k_e is proportional to electrical conductivity, it was increased with enhanced electrical conductivity by rGO content. However, the increase of electric thermal conductive factor had not affected significantly the total thermal conductivity behavior because the contribution of k_e was negligible in overall thermal conductivities, remaining at approximately 40 W/mK in all composite samples. On the other hand, the lattice factor by phonon transport was dominantly influenced on the total thermal conductivity in these composites. Lattice thermal conductivity is proportional to the effective mean free path (l) of phonon transport such as eq 7 (ν: the average velocity of medium, c_p: the specific heat capacity). It is negatively influenced by phonon scattering (boundary, impurity, phonon−phonon scattering), resulting in a decline of thermal conductivity.[39]

$$k_l = \frac{1}{3} l \nu c_p \tag{7}$$

In these composites, the interfaces between rGO nanosheets and WS_2 particles having 2D structure with a high surface area were considered to restrict an increase of thermal conductivity by inducing phonon scattering at the boundary with low effective mean free path of phonon transport. As a result, the figure of merit (ZT value), which express the efficiency of a thermoelectric material, was optimized to 6.8×10^{-4} at 0.8 wt % rGO sample, a 260% increase (1.9×10^{-4} in WS_2), as shown in Figure 5b. When 1 wt % rGO was contained in the composite, a decreased Seebeck coefficient resulted in a lower ZT value than that of the 0.8 wt % rGO sample. These enhanced ZT values were attributed to increased electrical conductivity by rGO channel producing electron transport path in the composites and to the steady thermal conductivity without further increase by the phonon scattering in 2D materials.

CONCLUSIONS

WS_2/rGO composites, as a function of the weight percentage of rGO, were fabricated in order to obtain optimized ZT values by SPS at 1473 K under vacuum conditions. In the SPS process, WS_2 sintering and the reduction of GO occurred simultaneously. In this composite, reduced GO formed transport paths for carriers when rGO was contained above 0.4 wt % of rGO in the composites with increased carrier concentration and mobility. This resulted in increased electrical conductivity of up to a maximum of approximately 3.0×10^3 (S/m) at 5 wt % rGO contained sample with decrease in the Seebeck coefficient to 1.9×10^1 (μV/K). By optimizing the electrical conductivity and the Seebeck coefficient, the highest power factor (8.7×10^1 μW/mK^2) was obtained with 0.8 wt % rGO. This value was 310% greater than that produced by WS_2 without rGO. Through these results, it has been confirmed that rGO provides a conductive path which can effectively transport charge carriers in WS_2/rGO composites. However, a large surface area of their 2D structures and a lot of interfaces between WS_2 particles and rGO nanosheets induced phonon scattering, and it makes an effective mean free path for phonon transport to be short, leading to the restriction of the increase in thermal conductivity. Thus, a thermal conductivity of WS_2/rGO composites remained around that of WS_2 without rGO (about 40 W/mK). With the values obtained for the power factor and thermal conductivity, an optimized ZT value was achieved at 0.8 wt % rGO contained sample; this value was 260% higher than that of WS_2 without rGO.

MATERIALS AND METHODS

The graphene oxide (GO) was prepared using graphite (SP-1, Bay Carbon Inc.); sodium nitrate ($NaNO_3$) (≥99.0% M, Sigma-Aldrich); potassium permanganate ($KMnO_4$) (≥99.0% M, Sigma-Aldrich); sulfuric acid (H_2SO_4) (95% M, Daejung Chemicals and Metals); hydrogen peroxide (H_2O_2) (30% M, Daejung Chemicals and Metals); and hydrochloric acid (HCl) (35% M, Daejung Chemicals and Metals). WS_2 (powder, 2 μm, 99%, Sigma-Aldrich) was used after being treated with ultrasonication (560 W) for 10 min.

The GO was obtained using Hummers' method.[40] First, graphite (1 g), H_2SO_4 (23 mL), and $NaNO_3$ (0.5 g) were stirred for 1 h in a round-bottom flask with an ice bath. Subsequently, $KMnO_4$ was added to the solution with stirring. The mixed solution was stirred for 1 h and then was maintained at 30 °C for 30 min, followed by dilution to 46 mg/mL by adding deionized water (DI water) gradually for 15 min. A mixture of H_2O and H_2O_2 (140 and 2.5 mL, respectively) was then added to the mixture and was stirred for 1 h. During this process, the color of the solution changed from black to brown. Once the color of the solution had changed, it was centrifuged repeatedly (at 8000 rpm for 10 min) with the mixture of HCl/H_2O (154 mL/385 mL) and H_2O. The sediment was then dried by freeze-drying for 12 h. The final step was the preparation of the GO suspension, which involved sonication of the sediment in DI water for 15 min.

WS_2/GO powders were obtained by vacuum filtration. To begin with, WS_2 particles were dispersed in ethanol (EtOH, 2 mg/mL) using ultrasonication (560 W, 10 min, VCX-750PS (750 watts), Sonics & Materials). The GO suspension (1 mg/mL) was then stirred into the WS_2 solution and was sonicated in a water bath for 5 min. In this process, the ratio of WS_2 and GO was determined by varying the content of GO (0−5 wt % of the GO sample). Following this, the mixture was filtered onto a poly(tetrafluoroethylene) (PTFE) membrane (0.2 μm, 47 mm, Merck Millipore). The filtered powder was sintered into a coin-shaped pellet from SPS with dimension of 30 mm in diameter and approximately 1 mm in thickness. After the powder was placed between graphite films in a graphite mold, SPS was performed under a pressure of 80 MPa in vacuum. Once the temperature of the mold reached 1473 K with a heating rate of 373 K/min, it was maintained for 1 min. The trace of the graphite films at the SPS process was removed by polishing from all of the samples. The naming convention of the samples was determined by the GO or rGO content (before sintering and reduction of GO: WS_2/0.2−5 wt % of GO sample; after sintering with reduction of GO: WS_2/0.2−5 wt % of rGO sample).

DOI: 10.1021/acssuschemeng.8b03949
ACS Sustainable Chem. Eng. 2018, 6, 15487−15493

To perform the morphology analysis of the GO, the GO suspension was deposited onto a Si wafer by spin-coating (1500 rpm, 30 s) and then was dried at 353 K in air. This Si wafer had been cleaned by piranha solution for 30 min before the deposition of the GO suspension. The thickness and size of the prepared GO were then characterized by atomic force microscopy (AFM, SPA400, SII) in a noncontact mode, using a Si tip (f = 320 kHz, C = 42 N/m, NCHR). The morphology of the WS_2/rGO composites was analyzed by field-emission scanning electron microscopy (JSM-7610F, JEOL Ltd.). WS_2 powder and mixture of WS_2 and GO were deposited onto a slide glass by drop-casting before being dried in the air at 353 K. WS_2/rGO composites, which were fabricated by SPS, were observed at perpendicular direction after polishing. To differentiate the rGOs in the composites, EDS mapping was used. The diffraction pattern of WS_2 was confirmed by an X-ray diffractometer (Xpert, Philips) with a Cu Kα radiation source (40 kV/200 mA, measurement range: 10−80°, step: 0.05°). A Raman spectrometer (high resolution Raman spectrometer, Renishaw) was used with 632.8 nm of laser source to confirm a reduction of GO. In this analysis, the composite film was prepared at a high load of rGO (5 wt % rGO sample) because samples with an amount of rGO smaller than 1 wt % had a very low peak intensity compared with that of WS_2; thus, it was difficult to observe their peaks. Measurement of the charge-carrier concentration and mobility was made using the Van der Pauw method. As a requirement for this method, four probes were placed at the corners of a two-dimensional isotropic sample (1 × 1 cm^2). Moreover, a magnetic field (0.556 T) and current (1 mA) were applied (Hall effect System, HMS-3000, Ecopia). The Seebeck coefficient and electrical conductivity were measured using a thermoelectric property measurement system (TFTEP-800, SEEPEL Co., Ltd., Keithley source-meter 2400, Agilent 34970A, Agilent 34420A). In this system, electrical conductivity was obtained by using the four-point-probe method, and the Seebeck coefficient was obtained using the potential difference (ΔV) by applied temperature gradient (ΔT = ±1 and 3 K) at room temperature. The thermal diffusivity of the samples was measured by laser flash method (LFA 447, NETZCH), and the thermal conductivity (k) was calculated via the thermal diffusivity (a), specific heat capacity (c_p), and density of materials (ρ) ($K = \rho c_p a$). The specific heat capacity was measured by using DSC 200 F3 (NETZCH).

■ ASSOCIATED CONTENT

Supporting Information

The Supporting Information is available free of charge on the ACS Publications website at DOI: 10.1021/acssuschemeng.8b03949.

Seebeck coefficient of WS_2/rGO composites by rGO content and the thermal conductivity of WS_2/rGO composites after SPS process (PDF)

■ AUTHOR INFORMATION

Corresponding Author

*E-mail: hyunjung@kookmin.ac.kr.

ORCID

Soohyun Kim: 0000-0002-7698-5198

Hyunwoo Bark: 0000-0002-4203-751X

Notes

The authors declare no competing financial interest.

■ ACKNOWLEDGMENTS

This research was supported by Basic Science Research Program through the National Research Foundation of Korea (NRF) funded by the Ministry of Science and ICT (NRF-2017R1A2B2010552 and 2015R1A5A7037615).

■ REFERENCES

(1) Bell, L. E. Cooling, Heating, Generating Power, and Recovering Waste Heat with Thermoelectric Systems. *Science* **2008**, *321* (5895), 1457−1461.

(2) Vining, C. B. An Inconvenient Truth about Thermoelectrics. *Nat. Mater.* **2009**, *8* (2), 83−85.

(3) Kraemer, D.; Poudel, B.; Feng, H. P.; Caylor, J. C.; Yu, B.; Yan, X.; Ma, Y.; Wang, X.; Wang, D.; Muto, A.; McEnaney, K.; Chiesa, M.; Ren, Z.; Chen, G. High-Performance Flat-Panel Solar Thermoelectric Generators with High Thermal Concentration. *Nat. Mater.* **2011**, *10* (7), 532−538.

(4) Kim, M. K.; Kim, M. S.; Lee, S.; Kim, C.; Kim, Y. J. Wearable Thermoelectric Generator for Harvesting Human Body Heat Energy. *Smart Mater. Struct.* **2014**, *23* (10), 105002.

(5) Kim, C. S.; Lee, G. S.; Choi, H.; Kim, Y. J.; Yang, H. M.; Lim, S. H.; Lee, S. G.; Cho, B. J. Structural Design of a Flexible Thermoelectric Power Generator for Wearable Applications. *Appl. Energy* **2018**, *214*, 131−138.

(6) Snyder, G. J.; Toberer, E. S. Complex Thermoelectric Materials. *Nat. Mater.* **2008**, *7* (2), 105−114.

(7) Dresselhaus, M. S.; Chen, G.; Tang, M. Y.; Yang, R.; Lee, H.; Wang, D.; Ren, Z.; Fleurial, J. P.; Gogna, P. New Directions for Low-Dimensional Thermoelectric Materials. *Adv. Mater.* **2007**, *19* (8), 1043−1053.

(8) Heremans, J. P.; Dresselhaus, M. S.; Bell, L. E.; Morelli, D. T. When Thermoelectrics Reached the Nanoscale. *Nat. Nanotechnol.* **2013**, *8* (7), 471−473.

(9) Kim, K. T.; Choi, S. Y.; Shin, E. H.; Moon, K. S.; Koo, H. Y.; Lee, G. G.; Ha, G. H. The Influence of CNTs on the Thermoelectric Properties of a CNT/Bi_2Te_3 composite. *Carbon* **2013**, *52*, 541−549.

(10) Li, J.; Tan, Q.; Li, J. F.; Liu, D. W.; Li, F.; Li, Z. Y.; Zou, M.; Wang, K. BiSbTe-Based Nanocomposites with High ZT: The Effect of SiC Nanodispersion on Thermoelectric Properties. *Adv. Funct. Mater.* **2013**, *23* (35), 4317−4323.

(11) Li, Z. Y.; Li, J. F.; Zhao, W. Y.; Tan, Q.; Wei, T. R.; Wu, C. F.; Xing, Z. B. PbTe-Based Thermoelectric Nanocomposites with Reduced Thermal Conductivity by SiC Nanodispersion. *Appl. Phys. Lett.* **2014**, *104* (11), 113905.

(12) Gandi, A. N.; Schwingenschlögl, U. WS_2 As an Excellent High-Temperature Thermoelectric Material. *Chem. Mater.* **2014**, *26* (22), 6628−6637.

(13) Solanki, G.; Gujarathi, D.; Deshpande, M.; Lakshminarayana, D.; Agarwal, M. Transport Property Measurements in Tungsten Sulphoselenide Single Crystals Grown by a CVT Technique. *Cryst. Res. Technol.* **2008**, *43* (2), 179−185.

(14) Kim, J.-Y.; Choi, S. M.; Seo, W.-S.; Cho, W. S. Thermal and Electronic Properties of Exfoliated Metal Chalcogenides. *Bull. Korean Chem. Soc.* **2010**, *31* (11), 3225−3227.

(15) Coleman, J. N.; Lotya, M.; O'Neill, A.; Bergin, S. D.; King, P. J.; Khan, U.; Young, K.; Gaucher, A.; De, S.; Smith, R. J. Two-Dimensional Nanosheets Produced by Liquid Exfoliation of Layered Materials. *Science* **2011**, *331* (6017), 568−571.

(16) Suh, D.; Lee, D.; Kang, C.; Shon, I.-J.; Kim, W.; Baik, S. Enhanced Thermoelectric Properties of Tungsten Disulfide-Multi-walled Carbon Nanotube Composites. *J. Mater. Chem.* **2012**, *22* (40), 21376−21381.

(17) Becerril, H. A.; Mao, J.; Liu, Z.; Stoltenberg, R. M.; Bao, Z.; Chen, Y. Evaluation of Solution-Processed Reduced Graphene Oxide Films as Transparent Conductors. *ACS Nano* **2008**, *2* (3), 463−470.

(18) Wang, X.; Zhi, L.; Müllen, K. Transparent, Conductive Graphene Electrodes for Dye-Sensitized Solar Cells. *Nano Lett.* **2008**, *8* (1), 323−327.

(19) Huh, S. H. Thermal Reduction of Graphene Oxide. *In Physics and Applications of Graphene-Experiments*; Mikhailov, S., Ed.; InTech: Rijeka, Croatia, 2011; pp 73−90.

(20) Chen, W.; Yan, L. Preparation of Graphene by a Low-Temperature Thermal Reduction at Atmosphere Pressure. *Nanoscale* **2010**, *2* (4), 559−563.

(21) Walker, L. S.; Marotto, V. R.; Rafiee, M. A.; Koratkar, N.; Corral, E. L. Toughening in Graphene Ceramic Composites. *ACS Nano* **2011**, *5* (4), 3182−3190.
(22) Fernández-García, L.; Suárez, M.; Menéndez, J. L.; Pecharromán, C.; Menéndez, R.; Santamaría, R. Dielectric Behavior of Ceramic−Graphene Composites Around the Percolation Threshold. *Nanoscale Res. Lett.* **2015**, *10*, 216.
(23) Brainard, W. A. *The Thermal Stability and Friction of the Disulfides, Diselenides, and Ditellurides of Molybdenum and Tungsten in Vacuum (10^{-9} to 10^{-6} Torr)*; NASA Technical Note TN D-5141; NASA: Washington, DC, 1968; pp 1−26.
(24) Kim, S. H. Influence of Sulfides on the Tribological Properties of Composites Produced by Pulse Electric Current Sintering. *Int. J. Miner., Metall. Mater.* **2014**, *21* (1), 95−103.
(25) Zhu, Y. T.; Manthiram, A. Influence of Processing Parameters on the Formation of WC-Co Nanocomposite Powder Using a Polymer as Carbon Source. *Composites, Part B* **1996**, *27* (5), 407−413.
(26) Xiao, T. D.; Tan, X.; Yi, M.; Peng, S.; Peng, F.; Yang, J.; Dai, Y. Synthesis of Commercial-Scale Tungsten Carbide-Cobalt (WC/Co) Nanocomposite Using Aqueous Solutions of Tungsten (W), Cobalt (Co), and Carbon (C) Precursors. *J. Mater. Sci. Chem. Eng.* **2014**, *2*, 1−15.
(27) Fan, J.; Zhuang, D.; Zhao, D.; Zhang, G.; Wu, M.; Wei, F.; Fan, Z. Toughening and Reinforcing Alumina Matrix Composite with Single-Wall Carbon Nanotubes. *Appl. Phys. Lett.* **2006**, *89* (12), 121910.
(28) Yan, Y.; Xia, B.; Qi, X.; Wang, H.; Xu, R.; Wang, J.-Y.; Zhang, H.; Wang, X. Nano-Tungsten Carbide Decorated Graphene as Co-Catalysts for Enhanced Hydrogen Evolution on Molybdenum Disulfide. *Chem. Commun.* **2013**, *49* (43), 4884−4886.
(29) Berkdemir, A.; Gutierrez, H.; Botello Mendez, A.; Perea Lopez, N.; Elias, A. Identification of Individual and Few Layers of WS_2 Using Raman Spectroscopy. *Sci. Rep.* **2013**, *3*, 1755.
(30) Peimyoo, N.; Shang, J.; Yang, W.; Wang, Y.; Cong, C.; Yu, T. Thermal Conductivity Determination of Suspended Mono- and Bilayer WS_2 by Raman Spectroscopy. *Nano Res.* **2015**, *8* (4), 1210−1221.
(31) Ferrari, A.; Meyer, J.; Scardaci, V.; Casiraghi, C.; Lazzeri, M.; Mauri, F.; Piscanec, S.; Jiang, D.; Novoselov, K.; Roth, S. Raman Spectrum of Graphene and Graphene Layers. *Phys. Rev. Lett.* **2006**, *97* (18), 187401.
(32) Xie, L.; Sha, J.; Ma, Y.; Han, J. Thermal Reduction of Graphene Oxide in Organic Solvents for Producing Colloidal Suspensions of Reduced Graphene Oxide Sheets. *Fullerenes, Nanotubes, Carbon Nanostruct.* **2013**, *21* (10), 901−915.
(33) Zhan, D.; Ni, Z.; Chen, W.; Sun, L.; Luo, Z.; Lai, L.; Yu, T.; Wee, A. T. S.; Shen, Z. Electronic Structure of Graphite Oxide and Thermally Reduced Graphite Oxide. *Carbon* **2011**, *49* (4), 1362−1366.
(34) Choi, E.-Y.; Han, T. H.; Hong, J.; Kim, J. E.; Lee, S. H.; Kim, H. W.; Kim, S. O. Noncovalent Functionalization of Graphene with End-Functional Polymers. *J. Mater. Chem.* **2010**, *20* (10), 1907−1912.
(35) Moon, I. K.; Lee, J.; Ruoff, R. S.; Lee, H. Reduced Graphene Oxide by Chemical Graphitization. *Nat. Commun.* **2010**, *1*, 73.
(36) Kobayashi, T.; Kimura, N.; Chi, J.; Hirata, S.; Hobara, D. Channel-Length-Dependent Field-Effect Mobility and Carrier Concentration of Reduced Graphene Oxide Thin-Film Transistors. *Small* **2010**, *6* (11), 1210−1215.
(37) Zhang, K.; Zhang, Y.; Wang, S. Effectively Decoupling Electrical and Thermal Conductivity of Polymer Composites. *Carbon* **2013**, *65*, 105−111.
(38) Rout, C. S.; Joshi, P. D.; Kashid, R. V.; Joag, D. S.; More, M. A.; Simbeck, A. J.; Washington, M.; Nayak, S. K.; Late, D. J. Superior Field Emission Properties of Layered WS_2-RGO Nanocomposites. *Sci. Rep.* **2013**, *3*, 3282.
(39) Kim, W. Strategies for Engineering Phonon Transport in Thermoelectrics. *J. Mater. Chem. C* **2015**, *3* (40), 10336−10348.
(40) Hummers, W. S.; Offeman, R. E. Preparation of Graphitic Oxide. *J. Am. Chem. Soc.* **1958**, *80* (6), 1339.

DOI: 10.1021/acssuschemeng.8b03949
ACS Sustainable Chem. Eng. 2018, 6, 15487−15493